PAPER

Thermally/mechanically robust anodic aluminum oxide (AAO) microheater platform for low power chemoresistive gas sensor

To cite this article: Byeongju Lee *et al* 2023 *J. Micromech. Microeng.* **33** 085011

View the article online for updates and enhancements.

Thermally/mechanically robust anodic aluminum oxide (AAO) microheater platform for low power chemoresistive gas sensor

Byeongju Lee[1] [iD]**, Incheol Cho**[1] [iD]**, Mingu Kang**[1] [iD]**, Daejong Yang**[2] [iD] **and Inkyu Park**[1,*] [iD]

[1] Department of Mechanical Engineering, Korea Advanced Institute of Science and Technology (KAIST), 291 Daehak-ro, Yuseong-gu, Daejeon 34141, Republic of Korea
[2] Department of Mechanical and Automotive Engineering, Kongju National University, 56 Gongjudaehak-ro, Gongju-si56 Gonjudaehak-ro, Gonju-si, Cheonan 31080, Republic of Korea

E-mail: Inkyu@kaist.ac.kr

CrossMark

Abstract

The semiconductor metal oxide gas sensors are getting high attention owing to their high sensitivities and fast responses. They require high temperature for the reaction with target gases, and suspended silicon membrane microheaters are typically used to reduce the heating power consumption. However, they have low durability for long-term uses, and high probability of fracture by thermal stress or mechanical impact. In this study, as an alternative to the silicon membrane microheater, anodic aluminum oxide (AAO)-based microheater platform gas sensor was fabricated for low power consumption and high thermal/mechanical stabilities. Nanoscale air gaps of the AAO substrate reduce the heat loss transferred to the substrate. Therefore, AAO-based microheater platforms do not require suspended structures sustained by very thin bridges, which dramatically enhances thermal/mechanical stabilities. The temperature of fabricated microheater platform reached to 250 °C by a heating power of 27.4 mW. The excellent thermal/mechanical stabilities of the AAO-based microheater platforms were verified by cyclic on-off and mechanical shock test. The pulsed heating operation was adopted, and it reduced the heating power consumption to 9 mW. The fabricated AAO-based gas sensors showed much higher responses to NO_2 gas compared to the SiO_2 membrane-based gas sensors.

Supplementary material for this article is available online

(Some figures may appear in colour only in the online journal)

---

* Author to whom any correspondence should be addressed.

1. Introduction

Demands for detecting and monitoring hazardous, toxic, and flammable gases are rising globally. The gas sensors are utilized in a variety of applications, including industrial gas leak detection; air pollution analysis; indoor air quality monitoring; breath-based disease diagnosis; and agriculture [1–4]. Recently, low-power, compact gas sensors have been actively developed for internet of things (IOT) applications like smart cities, homes, and factories. Among different kinds of gas sensors, semiconductor metal oxide (SMO) gas sensors use metal oxides as sensing materials and detect certain gases by measuring the resistance change brought on by a redox reaction between the metal oxide and target gases [5, 6]. Due to their simple fabrication, low cost, high sensitivity, compactness, and low power consumption, SMO gas sensors are one of the most promising candidates for gas sensors in the mobile platforms [7, 8].

In order to facilitate the redox process, SMO gas sensors are typically operated at high temperatures in the 200 °C–400 °C range, incorporating microheater platforms with Joule-heating. Silicon and ceramics have been mainly used as substrates for the microheater platform-integrated gas sensors. Among them, the micro-electro-mechanical system (MEMS)-based silicon microheater platform applies a suspended microstructure by removing the bottom of the heating membrane in order to reduce heat transferred to the substrates using an etching process [6, 9–17]. The suspended microheater platform has been widely used including commercial SMO gas sensors owning to high heating efficiency. However, it has a critical limitation of low mechanical stability caused by extremely thin bridge structures supporting the heating membrane. The suspended microheater platform can be easily damaged by thermal stresses and mechanical vibrations, which inhibits their wide usage in practical applications [18]. The ceramic substrate has a significantly lower thermal conductivity than silicon, thus ceramic-based microheaters can achieve comparable levels of heating efficiency without formation of the floating structure [19, 20]. However, the microfabrication of ceramic-based microheater using conventional MEMS process is not easy, which makes micro-scale patterning and mass production difficult.

Anodic aluminum oxide (AAO) is a self-organized and highly ordered material with nanoscale air pore structures. Since the air pores suppress horizontal heat flow, the amount of heat transferred to the substrate is drastically reduced [21]. Since the AAO substrate has much lower thermal conductivity ($0.53–1.62$ W mK^{-1}) than silicon (130 W mK^{-1}), an AAO-based microheater exhibits high energy efficiency [22]. MEMS fabrication process can be used for AAO substrate, and furthermore, the high aspect ratio vertical etching process is extremely simple owing to the columnar pores. Recently, several studies reported the AAO-based microheater platforms [23–26] and SMO gas sensors [27, 28]. However, most of the research focused on reducing power consumption, not the robustness (table 1). For practical applications, high-stability of the sensor platform should be considered together.

Thus, we designed AAO-based microheater platform, and carried out stability tests to verify the robustness of our platform.

In this study, we designed and fabricated a SMO gas sensor based on the AAO microheater platform and applied the MEMS technology to overcome the stability issue of the silicon membrane-based microheater platform (figure 1(a)). In order to further cut down the heating power consumption, the microscale air gap patterns were formed between the heating plate and heat sink on the AAO substrate (figure 1(b)). The fabricated microheater was supported by bridges with the same thickness as the AAO substrate, which provides high thermal and mechanical stability while operating with low power consumption. The SMO gas sensors used metal oxide sensing materials (WO_3, In_2O_3) deposited by the glancing angle deposition (GLAD) method, which formed porous structures and showed high gas sensitivity (figure S1) [13, 29, 30]. Finally, the gas detection performances were evaluated by gas tests with a nitrogen dioxide (NO_2), and the same gas test was performed while applying pulsed heating, realizing high-stability and low-power gas sensors.

2. Experimental section

2.1. Sensor platform fabrication

Figure 2 illustrates the fabrication process of the SMO gas sensor based on the AAO microheater platform. For the gas sensor fabrication, we used a commercial AAO substrate (InRedox, USA) with a size of 1×1 cm^2, a thickness of 150 μm, a pore diameter of 40 nm, an inter-pore distance of 105 nm, and a porosity of 15%. First, an electron beam (E-beam) evaporator was used to deposit a Cr layer (100 nm) on the bare AAO chip in order to apply UV photolithography. If the photoresist is directly coated on the AAO surface, the photoresist enters into air pores and hinders the following MEMS process. Cr layer blocks pores so that photoresist can be uniformly deposited on the substrate. Polydimethylglutarimide and photoresist (AZ 5214, MicroChemicals, Germany) were spin-coated and patterned by UV photolithography for heater electrode patterning. The exposed Cr layer was removed by a commercial Cr etchant (Cr-7, Cyantek Corporation, USA). Next, a Ta/Pt (20/200 nm thickness) heater electrode was deposited by RF-sputtering and patterned by the liftoff process. Ta film was used as an adhesion layer as well as a buffer layer between an AAO substrate and a Pt layer. Remaining Cr layer was completely removed by a Cr etchant. Schematic diagrams of lift-off process using Cr layer are illustrated in figure S2. After heater electrode deposition, SiO_2 layer of 800 nm thickness was deposited by plasma-enhanced chemical vapor deposition (PECVD) on the patterned heater electrode layer for patterning and insulation between the heater and sensing electrodes. The SiO_2 insulation layer was patterned with a photoresist (AZ9260, MicroChemicals, Germany), then selectively etched by reactive ion etching (RIE) for electrical probing

| Substrate	Heater type	Heating area (μm^2)	Operating temperature (°C)	Power consumption (mW)	Stability test	References
Si/SiO$_2$	Suspended structure	3×100	300	6.9	△	[6]
Poly-Si/SiNx	Suspended structure	6×100	300	5.7	X	[9]
Si/SiO$_2$/SiN$_x$	Suspended structure	100 (circle)	327	30	X	[10]
Si/SiN$_x$	Suspended structure	250×250	400	39	X	[12]
Si/SiO$_2$	Suspended structure	100×100	250	11	△	[13]
Si/SiO$_2$	Suspended structure	300×300	300	210	X	[17]
Si/SiC	Closed membrane	50×50	500	20	X	[45]
Glass	Closed membrane	1000×1000	498	2350	△	[20]
Si/ITO/SiO$_2$	Closed membrane	290×290	350	386	X	[46]
Si/SiN$_x$/SiO$_2$	Closed membrane	200×200	400	250	○	[47]
Si/SiO$_2$	Suspended structure	50×50	400	11.8	○	[48]
Si/SiN$_x$	Suspended structure	250×100	440	36	○	[49]
AAO	Closed membrane	250×400	450	90	X	[26]
AAO	Suspended structure	500 (circle)	725	50	X	[25]
AAO	Closed membrane	600×600	200	40	X	[27]
AAO	Suspended structure	125×125	250	27.4	○	This work

※ Stability test – X: Not tested, △: Tested for steady-state heating, ○: Tested for pulsed heating
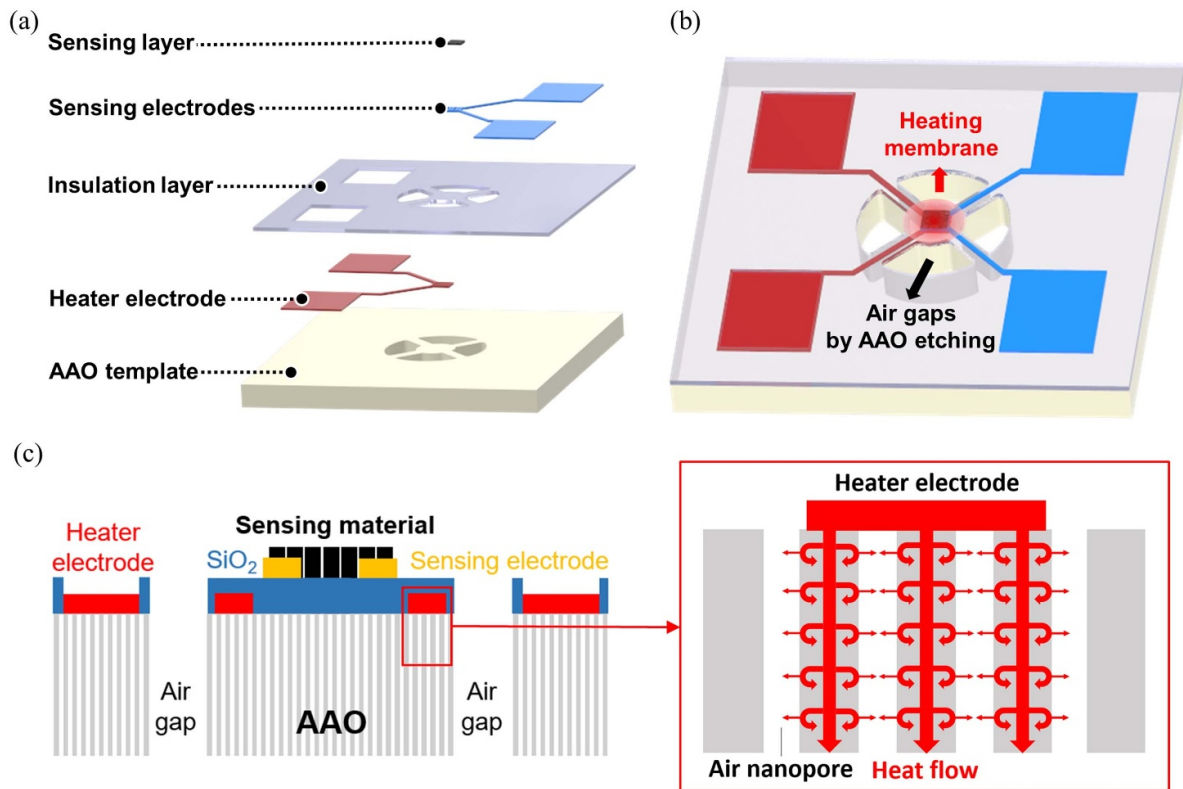
Figure 1. Schematic diagrams of the semiconducting metal oxide (SMO) gas sensor integrated on an anodic aluminum oxide (AAO)-based microheater platform. (a) Illustrations of whole layers of the SMO gas sensor, and (b) fabricated SMO gas sensor. (c) Schematic diagram of the heat transfer mechanism for AAO microheater platform. Air nanopores of the AAO suppress horizontal heat loss inside the substrate.

of the heater electrode. A Cr/Au (20/200 nm thickness) layer was deposited by an E-beam evaporator, which forms interdigitated sensing electrodes. After the deposition of electrodes, the etching window was patterned by photolithography, and the SiO$_2$ layer was etched by RIE. Next, air gap patterns were fabricated for reduction of the heating power consumption. The precise formation of the air gap patterns

can be available by a wet etching process. The exposed AAO substrate was wet-etched in 10 wt% phosphoric acid for 90 min. Finally, sensing materials were deposited on the heating microplate through GLAD via RF sputtering. Two types of high-purity sputtering targets (WO$_3$, In$_2$O$_3$) were used for the sensing material deposition. The tilting angle between the sputtering target and substrate was set to 85°. The base
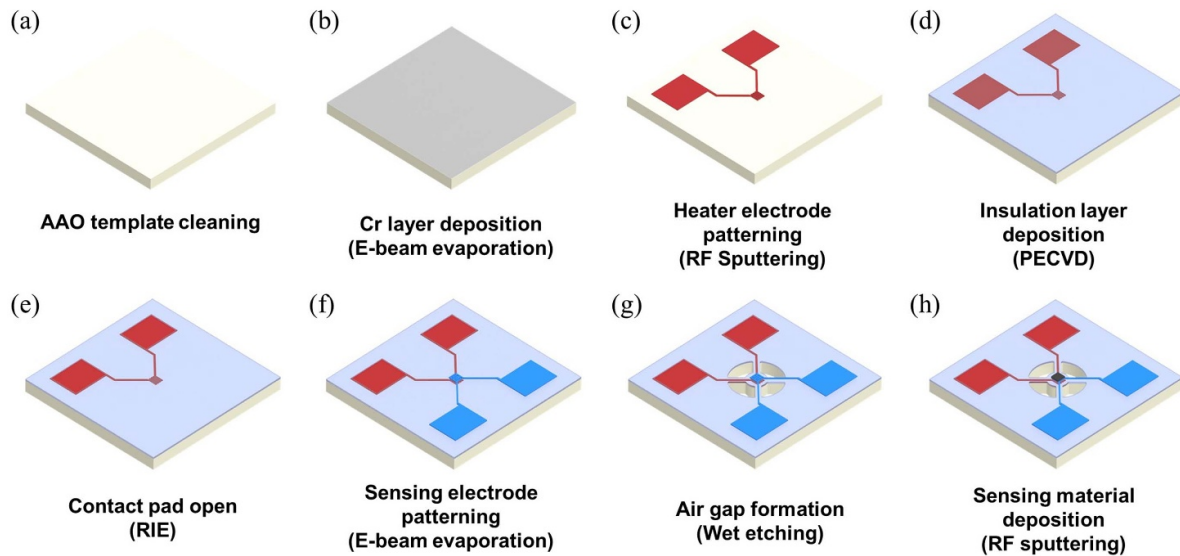
Figure 2. Fabrication processes of AAO microheater platform gas sensor: (a)–(c) Cr layer deposition for heater electrode patterning; (d), (e) SiO$_2$ layer deposition and patterning for insulation and probing; (f) sensing electrode patterning; (g) air gap formation by wet etching method; (h) sensing material deposition by glancing angle deposition through RF sputtering. Color codes: AAO (white), chromium (gray), tantalum/platinum (red), silicon oxide (sky blue), chromium/gold (blue), sensing material (black). The detailed processes are demonstrated in the text.

pressure, ambient gas, gas flow rate, rotation speed, and RF power were 4 mTorr, 100% Ar condition, 50 sccm, 3.6 rpm, and 250 W, respectively. The sputtering time was set to deposit a ∼200 nm thick film. For this, WO$_3$ and In$_2$O$_3$ thin films were deposited for 120 and 90 min, respectively.

2.2. Characterization of microheater platform

Numerical simulation (COMSOL Multiphysics®) and resistive temperature detection (RTD) were conducted to measure the relationship between power consumption and heating temperature. The resistance of the Pt heater electrode was measured under external heating conditions using a hot-plate and Joule heating conditions using a source meter (Keithley 2400, Tektronix, USA). Infrared micro-thermography was used to analyze the temperature distribution of the AAO microheater platform and the measurement was carried out by connecting to the copper plate for precise adjustment of the temperature of the AAO substrate (figure S5(a)) [31]. Thermal/mechanical stabilities of fabricated AAO microheater platform were verified by pulsed heating operation test and impact cycle test. Comparison experiments were performed using silicon-based microheater platforms fabricated in earlier studies for the thermal/mechanical stability tests [13]. In the pulsed heating operation test, on-off cycles were repeatedly performed during which a voltage was applied for 1 s and turned off for 1 s. The voltage was applied so that the heating microplate would reach a temperature of ∼500 °C. The impact cycle test was conducted by transmitting an impact using a pendulum connected with a hammer. During the impact cycle test, the power consumption of each microheater platform was measured in real time by connecting to PCB circuits with same dimensions.

2.3. Characterization of sensing materials

To compare the sensing performance of the AAO-based gas sensors and Si-based gas sensors, the sensing materials were deposited on the Si-based microheater platforms under the same GLAD deposition conditions. The surface morphologies and x-ray diffraction (XRD) patterns of metal oxide thin films were analyzed through ultra-high resolution scanning electron microscope (UHR-SEM, SU-8230, Hitachi, Japan) and thin film x-ray diffractometer (SmartLab, RIGAKU), respectively. The diffractometer uses a PhotonMax high-flux 9 kW rotating anode x-ray source coupled with a Hypix-3000 high-energy-resolution. For the sensing performance analysis, we applied the input voltage to heater platforms to reach the heating temperature to 250 °C, and measured heater resistance using a Keithley 2400 source meter. The resistance of sensing materials was measured by another source meter (Keithley 2635a, Tektronix, USA) with an input voltage of 2.0 V. Nitrogen dioxide (NO$_2$) was selected as a target gas for gas sensing performance test. NO$_2$ is a highly reactive and toxic gas that is significant air pollutant [32, 33]. It is primarily emitted from combustion processes, such as vehicle emissions, power plants, and factories. In addition, NO$_2$ is one of the major contributors to acid rain, and exposure to over 1 ppm of NO$_2$ causes respiratory diseases. The fabricated gas sensor was located in a custom-made gas chamber and the gas flow was precisely adjusted using mass flow controllers (AFC500, Atovac, Korea). By balancing the flow of the N$_2$, O$_2$, and NO$_2$ gases, the NO$_2$ concentration range from 0.5 to 5 ppm was precisely controlled. Before each gas test, the gas chamber was stabilized under air conditions (80% N$_2$, 20% O$_2$) for 3000 s. Next, NO$_2$ was exposed for 1,000 s and recovered under air conditions for 1000 s.
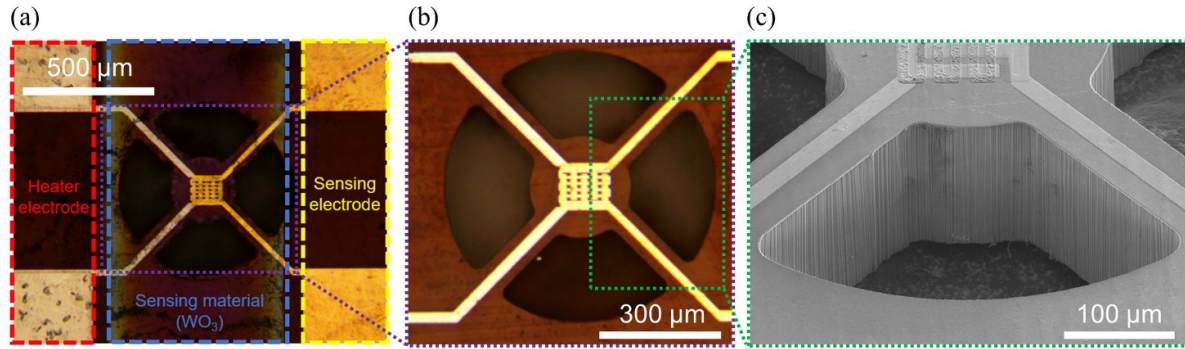
Figure 3. Optical images of the fabricated AAO microheater platform gas sensor with formation of air gap patterns. The microheater has 250 μm of diameter, and the bridges have a width of 70 μm. (a) Optical microscopic image of the fabricated gas sensor deposited with WO$_3$, (b) magnified image of the microheater of the air gap pattern, (c) magnified SEM image of the microheater platform and the air gap pattern.

3. Results and discussion

Figure 3 shows the AAO microheater platform-integrated gas sensor. A PECVD SiO$_2$ layer entirely separated the heater electrode from the sensing electrode, and the contact pads of the heater electrode were opened for the electrical contact. The metal oxide thin films deposited by GLAD create an electrical connection across the 10 μm gaps between the sensing electrodes. Figure 3(a) is an optical microscopic image of the gas sensor with a WO$_3$ thin film. One sensor has a size of 1.5 × 1.5 mm^2, and the heating microplate heated by the microheater platform has a diameter of 250 μm. Figures 3(b) and (c) show magnified optical microscopic image of the heating microplate and SEM image of the air gap pattern, respectively. The air gap patterns were etched from 250 μm to 500 μm in a circular shape centered on the heating microplate connected through bridge structures with a width of 70 μm. The thickness of the bridges is 150 μm, which is same thickness with the bare AAO substrate. Based on previous research, etching mechanism of the AAO substrate was used for the formation of air gap patterns [34]. According to this mechanism, the etchant penetrates through the pores of the AAO substrate and removes their sidewalls uniformly, regardless of the depth from the surface. Therefore, vertical structures can be easily formed by wet etching of the AAO substrate.

Figure 4 shows the heating performances of fabricated AAO-based microheater platform. We measured the heating power consumption of the microheater platform floating in the air using the RTD test method. The resistance of the heater electrode was precisely measured under two different conditions. Under the external heating condition, the entire sensor chip was heated with a hot-plate. In contrast, under the Joule heating condition, the microheater platform was locally heated to a high temperature. As shown in figure S4, the resistance ratio of the heater electrode was calculated by numerical simulation, and the calibration was performed using the results [6]. Figures 4(a) and (b) show the changes of R_M (resistance on the heating microplate) under the external heating and Joule heating conditions, respectively. Figure 4(c) shows the relationship between heating power consumption and the temperature of the microplate by comparison between the results of the external heating and Joule heating conditions. As a result, the power consumption required for the heating microplate to rise to 250 °C was estimated as 27.4 mW. Figure 4(d) shows the temperature distribution analyzed by the numerical simulation. The three-dimensional model of the AAO-based microheater platform for the numerical simulation is illustrated in figure S3. The physical properties of the AAO substrate for the numerical simulation were employed from the previous research [22, 35–39], summarized in table S1. As a numerical simulation result, 24.0 mW was required for heating to 262 °C. The graph in figure 4(e) compares the power consumption—heating temperature relationships estimated by the RTD test and the numerical simulation, which shows proximity between these values. The temperature distribution was measured by infrared micro-thermography as shown in figure S5(b). The result shows that air gap structures allow microheater platform to locally heat the functional area with high efficiency.

Figures 5(a) and (b) show the resistance changes of the heater electrodes of the AAO-based and Si-based microheaters, respectively, under pulsed heating operation test. The microheaters of the two substrates were operated at a power to achieve a maximum temperature of 500 °C. The heating power consumption were 59 mW for AAO-based microheater and 26 mW for Si-based microheater, respectively. In the case of AAO-based microheater, the resistance of the heater electrode showed less than 1% variation after 150 000 cycles. On the contrary, Si-based microheater failed before 600 cycles, as shown in figure 5(b). As a result, it was verified that the AAO-based microheater is more thermally stable than the Si-based microheater. The results of impact cycle test are shown in figures 5(c) and (d). The impact cycle test setup and test samples are shown in figure S6. The impact cycle test was repeated by 100 cycles, and the heating temperature of both microheaters was maintained at 250 °C. The impact energy delivered to the sensor platform for each cycle was 0.158 J, similar to that of dropping at 1 m height. As shown in the graphs, all four AAO-based microheaters operated stably during 100 impact cycles without significant changes of the
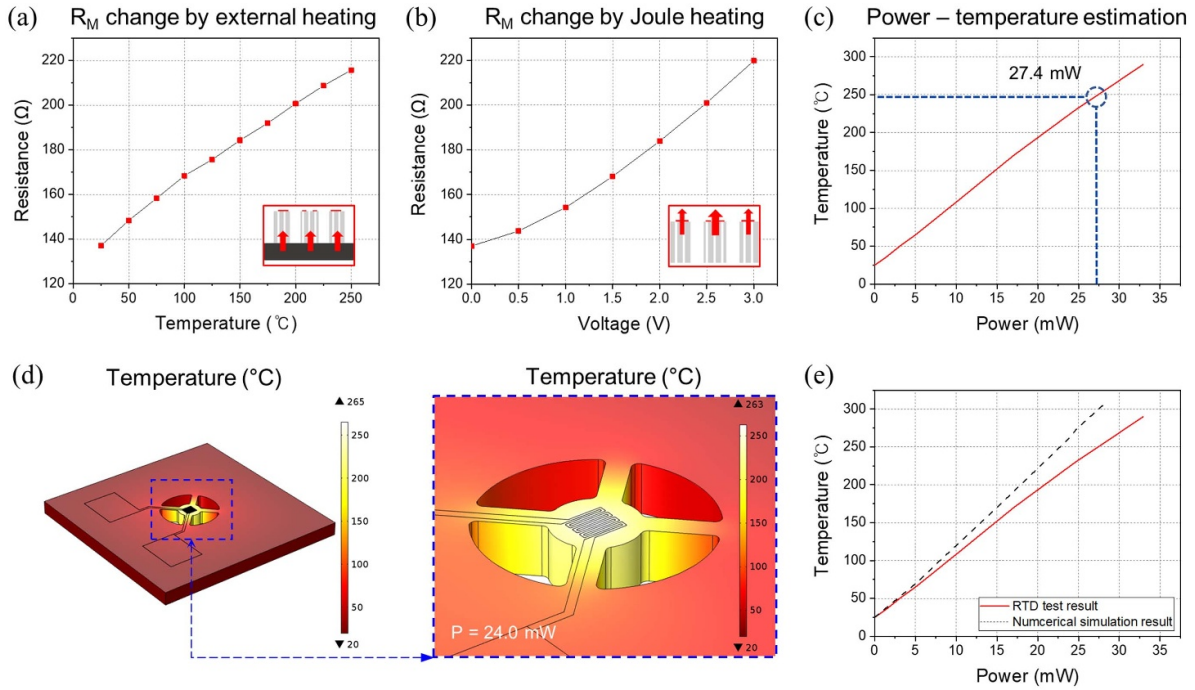
Figure 4. Characterization results of the fabricated microheater platform. (a) Change of the heater resistance on the heating membrane induced by external heating. (b) Change of the heater resistance on the heating membrane induced by Joule heating. (c) Estimated power–temperature relationship from the experimental data. (d) Result of the numerical simulation for calculation of the heating power consumption. (e) Comparison of power consumption—heating temperature relationship between the RTD test and the numerical simulation results.

heating power, while three out of four Si-based microheaters failed at 32, 45 and 70 impact cycles. In addition, they showed large changes in power consumption and operated unstably before they were completely broken down. The reason for the high stability of AAO-based microheater is the effect of thick bridge structures supporting the heating microplate. The AAO-based microheater platform has a much thicker heating microplate (150 μm) than the silicon-based microheater platform ($\sim$1 μm). Assuming that the bridge is simplified as a beam structure, the transverse force required for fracture is 22 500 times higher than that of the Si-based microheater since the AAO-based microheater is supported by 150 times thicker beam. Table 1 summarizes the characteristics of microheater platforms reported in other research. This work reduced the heating power consumption by half compared to recently reported AAO-based gas sensor platform [27], and achieved similar levels to commercial SMO gas sensors [40].

Figures 6(a)–(d) show the UHR-SEM images of metal oxide thin films deposited by the GLAD method. WO_3 and In_2O_3 has nanocolumnar structures on the AAO-based microheater platforms (figures 6(a) and (b)) and the Si-based microheater platforms (figures 6(c) and (d)). As shown in figures 6(a) and (b), the metal oxides deposited on the AAO-PECVD SiO_2 surface forms large nanocluster structures because the deposited SiO_2 layer blocks the air gaps of the AAO substrate. The nanoclusters have gap distance of 5–15 nm, and their diameters ranged from 150 to 300 nm. The porosity of the WO_3 and In_2O_3 thin films were $11.52 \pm 0.88\%$

and $12.46 \pm 1.18\%$, respectively. In the case of deposition on the Si substrates, metal oxide thin films deposited on a flat surface formed a nanorod structure with a smaller diameter, as shown in figures 6(c) and (d). The diameter and gap distance ranges are 20–60 nm and 5–15 nm, respectively. The porosity of the WO_3 thin film was $12.47 \pm 1.02\%$, and that of the In_2O_3 thin film was $11.25 \pm 1.27\%$. Through the surface morphology analysis, it was confirmed that the thin films deposited on the two substrates have similar porosity, but different nanostructures.

Figures 7(a) and (b) show the XRD patterns of metal oxide thin films deposited on the AAO and Si substrates. Both of metal oxide thin films were annealed at 400 °C for 2 h in the air to achieve crystalline structures. As shown in figure 7(a), both XRD patterns of the WO_3 thin films have similar diffraction peaks, and matches to the monoclinic phase pattern [41]. Also, as shown in figure 7(b), XRD patterns of the In_2O_3 thin films deposited on AAO and Si-based microheater platforms show almost the same peaks and intensities. The XRD patterns reveal cubic In_2O_3 crystalline phase [42]. Therefore, it was verified that the WO_3 and In_2O_3 thin films form the same crystalline structure on different substrates.

In the gas detection performance analysis, a NO_2 gas was exposed with the gas test setup illustrated in figure S7. The response of the gas sensor was defined as R_{gas}/R_{air}, where R_{gas} is the resistance of the sensing material exposed to NO_2 gas, and R_{air} is the resistance in the ambient air condition. The operating temperatures of both microheater
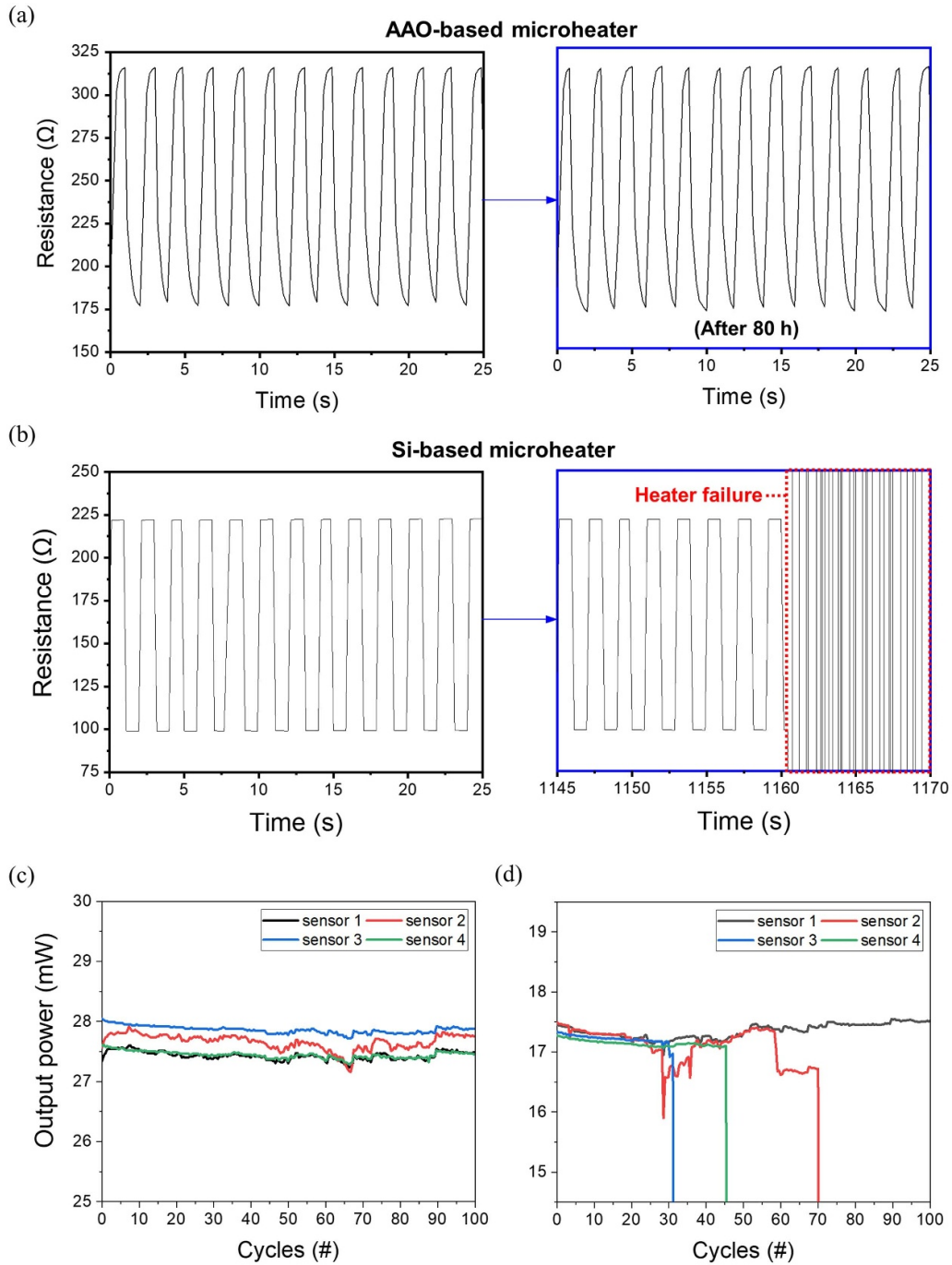
Figure 5. Thermal/mechanical reliability test results of AAO microheater and silicon-based microheater platforms. Pulsed heating test results of (a) AAO microheater platform and (b) Si microheater platform heated to 500 °C. Real-time measurement results of output power of (c) AAO microheater platform and (d) Si microheater platform during impact cycle test.

platforms was 250 °C (27.4 mW for AAO-based microheater and 11.5 mW for Si-based microheater). Figures 8(a) and (b) show the dynamic responses of the WO$_3$ gas sensors fabricated on AAO-based and Si-based microheater platforms. WO$_3$ deposited on the AAO-based microheater platform shows much higher responses (e.g. R_{gas}/R_{air} = 19.1 at 0.5 ppm; R_{gas}/R_{air} = 67.4 at 5 ppm) than that deposited on the Si-based microheater platform (e.g. R_{gas}/R_{air} = 1.12 at 0.5 ppm; R_{gas}/R_{air} = 2.83 at 5 ppm). Figures 8(c) and (d) show the

dynamic responses of the In$_2$O$_3$ gas sensor fabricated on AAO-based microheater and Si-based microheater. Similarly, In$_2$O$_3$ deposited on AAO-based microheater platform shows much higher responses (e.g. R_{gas}/R_{air} = 34.8 at 0.5 ppm; R_{gas}/R_{air} = 331.0 at 5 ppm) than deposited on Si-based microheater (e.g. R_{gas}/R_{air} = 6.6 at 0.5 ppm; R_{gas}/R_{air} = 75.9 at 5 ppm). The dynamic responses of the four gas sensors with real measured resistances are illustrated in figure S8. Figures 8(e) and (f) summarize the responses of the WO$_3$
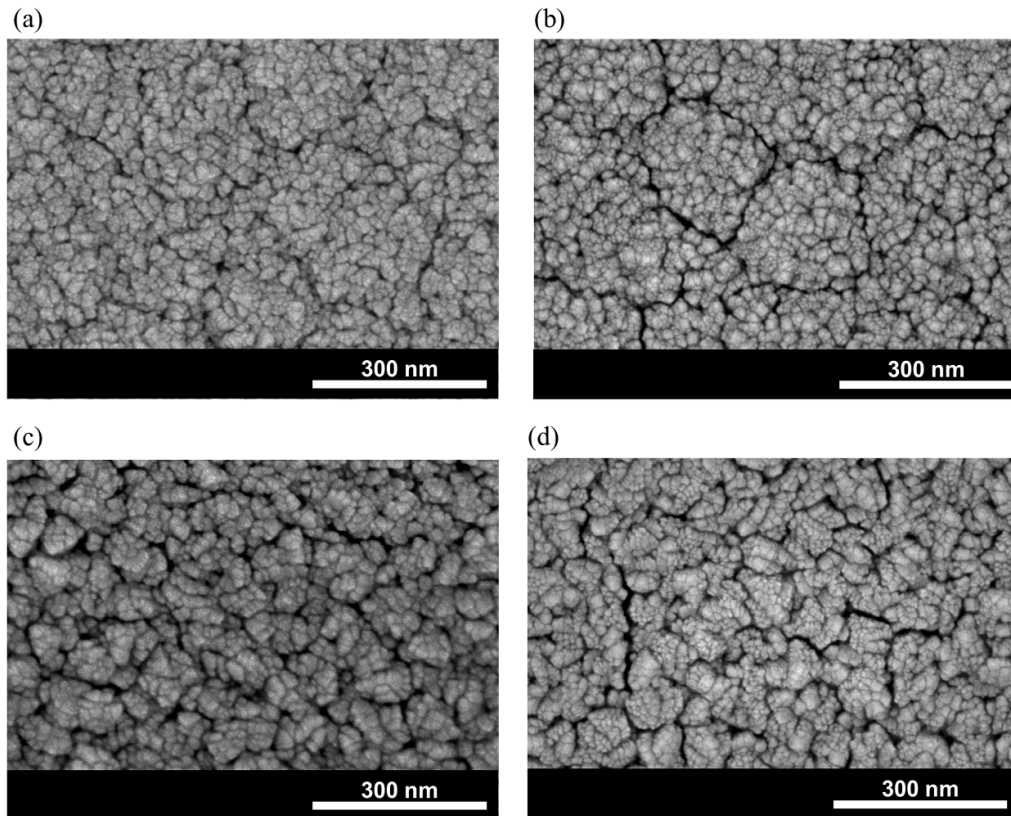
Figure 6. UHR-SEM images of metal oxide thin films deposited by a GLAD method. (a) WO_3 on AAO-SiO$_2$, (b) In_2O_3 on AAO-SiO$_2$, (c) WO_3 on Si, and (d) In_2O_3 on Si.
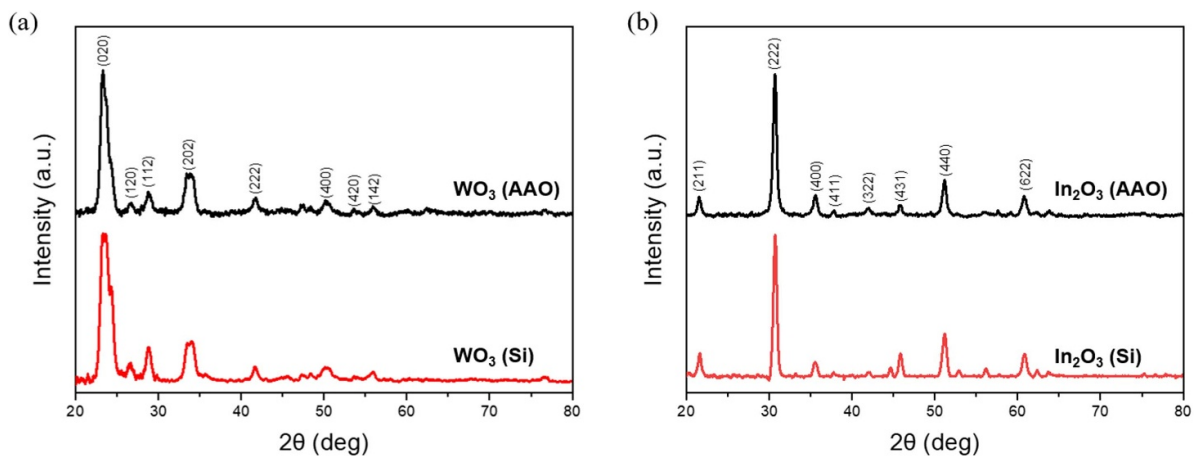

Figure 7. XRD patterns of metal oxide thin films with different substrates. (a) WO_3 and (b) In_2O_3.

gas sensors and In_2O_3 gas sensors. The sensitivities of the AAO-based gas sensors were higher than those of Si-based gas sensors at all gas concentration ranges, and In_2O_3 gas sensors showed higher responses than those of WO_3 gas sensors. The response time is defined as the time taken by the sensor to reach 90% of the equilibrium state after exposing target gas, and recovery time is defined as the time taken by the sensor to return to 90% of the base resistance in the air condition. Figure S10 summarized the response and recovery times of the sensors. Among the sensor tested, the WO_3 deposited on

AAO-based microheater exhibited the shortest response and recovery times.

The reason for improvement of the sensing performance of the AAO-based gas sensors can be explained by the grain boundary formation. The sensing mechanism of the SMO gas sensor involves measuring the resistance change caused by the oxidation-reduction reaction with oxygen ions [5]. This resistance change occurs due to the variation in the potential barrier height at the grain boundary. Therefore, the resistance change induced by the target gas is enhanced as the number
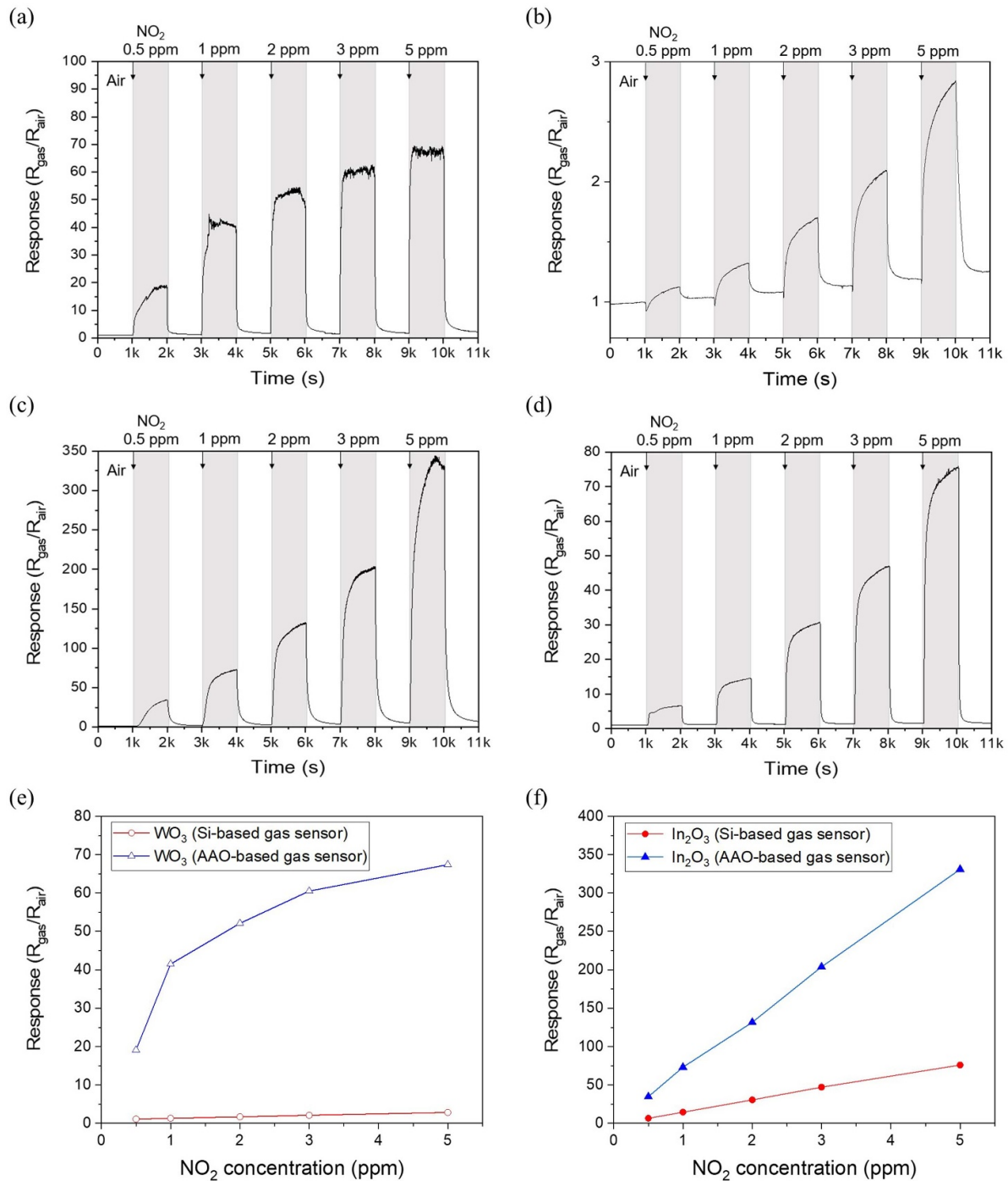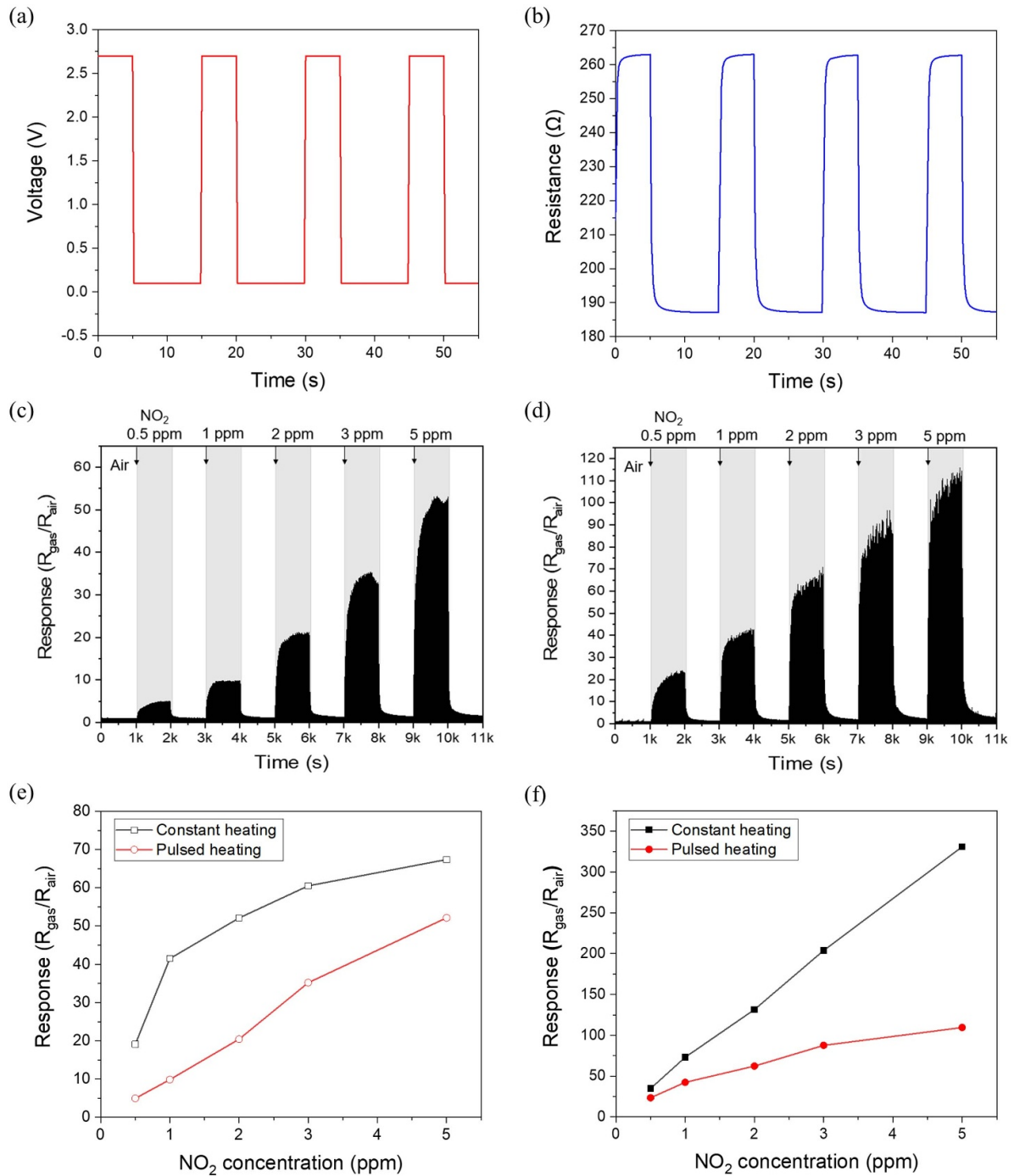
Figure 8. NO$_2$ gas sensing test results of sensors fabricated on AAO and Si-based microheaters with 250 °C heating conditions. (a) Dynamic response of WO$_3$ on AAO, (b) dynamic response of WO$_3$ on SiO$_2$, (c) dynamic response of In$_2$O$_3$ on AAO, and (d) dynamic response of In$_2$O$_3$ on SiO$_2$. Response comparison between AAO gas sensor and SiO$_2$ gas sensor deposited with (e) WO$_3$ and (f) In$_2$O$_3$.

of grain boundaries increases, and experimental verifications have been done in previous studies [43, 44]. As shown in figure 6, the sensing layers formed on the Si substrate and AAO substrate exhibit similar grain sizes. However, due to the honeycomb-like structure of the AAO substrate, it was observed that lager-sized nanoclusters were formed on the AAO surface. The nanocluster structures on the AAO leads to a higher density of grain boundaries compared to the nanorod structures formed on the Si substrate. This is supported by the

significantly higher base resistance of the sensing layer deposited on the AAO substrate, as shown in figure S8.

Next, we evaluated additional stabilities of the WO$_3$ gas sensor, which exhibited rapid and stable response to NO$_2$. As shown in figure S11(a), the repeatability test was carried out by 1 ppm and 2 ppm of NO$_2$, and it was verified that the gas sensor exhibited high stability to repeated exposure and recovery. Figure S11(b) presents the result of the long-term stability test for 1 ppm NO$_2$ gas. The response was evaluated

Figure 9. NO_2 gas sensing test results of AAO gas sensors operated by pulsed heating modes. (a) Applied voltage, (b) measured resistance of heater electrode. The duty cycle of applied pulsed heating mode was 1/3, and heating temperature was 250 °C. (c) Dynamic response of WO_3, and (d) dynamic response of In_2O_3 with a pulsed heating mode. Response comparison between constant heating and pulsed heating operation modes of (e) WO_3 gas sensors, (f) In_2O_3 gas sensors.

hourly over a period of 72 h, and the resulting error (standard deviation/mean × 100%) was measured at 1.3%. Figure S12 shows the gas selectivity test result with 10 ppm of acetone, 1.5 ppm of ammonia, 10 ppm of methane, and 1 ppm of nitrogen dioxide. The WO_3 sensor exhibited significantly higher response to NO_2 gas as compared to other gases, confirming its high selectivity to NO_2 gas.

By taking the advantage of the high thermal/mechanical stability of the AAO-based microheater platform, we could decrease the heating power consumption through pulsed heating operation mode. Figure 9(a) shows applied voltage to the heater electrode under pulsed heating operation. The period of the pulse was 15 s, where on-state was 5 s (2.7 V, ∼27 mW) and off-state was 10 s (0.1 V, ∼0.05 mW). Therefore, the total

heating power consumption was reduced to 9 mW. Figure 9(b) shows the change of the heater resistance under pulsed heating operation. The resistance change, which indicates temperature change of the heating microplate, has a transient region of 0.2 s. Figures 9(c) and (d) show the dynamic responses of WO_3 and In_2O_3 deposited on AAO-based microheater platforms. Similar with the constant heating condition, the responses of a WO_3 gas sensor (e.g. R_{gas}/R_{air} = 4.95 at 0.5 ppm; R_{gas}/R_{air} = 52.2 at 5 ppm) are lower than those of an In_2O_3 gas sensor (e.g. R_{gas}/R_{air} = 23.4 at 0.5 ppm; R_{gas}/R_{air} = 109.5 at 5 ppm). Figure S9 shows real measured resistance values of the WO_3 and In_2O_3 gas sensors under pulsed heating conditions. The responses under the constant heating condition and pulsed heating condition are summarized in figures 9(e) and (f). The sensitivity of the two sensors under pulsed heating condition is lower than that under the steady-state condition, but both sensors show much higher responses than Si-based gas sensors. Additionally, as shown in figure S13, it was observed that under pulsed heating condition, the response time ($\sim$200 s) and recovery time ($\sim$90 s) remained consistent. This suggests that the sensor's performances in terms of response and recovery is stable and predictable under pulsed heating condition. In summary, high-sensitivity gas sensors with power consumption of less than 10 mW were realized by taking advantage of high thermal/mechanical stability of AAO microheater platform and pulsed heating operation.

4. Conclusions

In this study, we suggested a low-power and high-stability gas sensor using an AAO-based microheater platform. The structure of the microheater platform gas sensor and a fabrication process applicable to the AAO substrate were developed. The fabrication process includes patterning layer deposition for photolithography; SiO_2 insulation layer deposition for electrode patterning; and air gap formation by wet etching. Using etching mechanism of the AAO substrate, bridge structures with a same thickness as the substrate could be easily fabricated. Two types of metal oxides (WO_3, In_2O_3) were selected as sensing materials and they formed nanocolumnar thin films by deposition through the GLAD method. As a result, we successfully fabricated SMO gas sensors based on AAO microheater platforms. The microheater platforms showed excellent thermal and mechanical stability because the heating platform used the entire thickness of the substrate, instead of microscale thin membrane configuration. NO_2 was used as a target gas for the gas sensing performance test, and the gas sensors on the AAO microheater platform showed much higher sensitivities than those on the Si-based microheater platform. The heating power could be further reduced by applying a pulsed heating operation owing to the stability of the microheater platform, and the gas sensors exhibited high level of sensitivities. By overcoming the stability limitations of previous Si-based microheaters, the gas sensor based on AAO microheater platform can be used in thermally/mechanically harsh environments. It also appears to be very suitable for long-term and portable gas monitoring systems owing to the high stabilities and sensitivities.

ORCID iDs

Byeongju Lee ⬤ https://orcid.org/0009-0003-6923-987X
Incheol Cho ⬤ https://orcid.org/0000-0002-9909-905X
Mingu Kang ⬤ https://orcid.org/0000-0002-0837-7254
Daejong Yang ⬤ https://orcid.org/0000-0002-8774-5843
Inkyu Park ⬤ https://orcid.org/0000-0001-5761-7739

References

[1] Mirzaei A, Leonardi S G and Neri G 2016 Detection of hazardous volatile organic compounds (VOCs) by metal oxide nanostructures-based gas sensors: a review *Ceram. Int.* **42** 15119–41

[2] Lee J, Jung Y, Sung S H, Lee G, Kim J, Seong J, Shim Y S, Jun S C and Jeon S 2021 High-performance gas sensor array for indoor air quality monitoring: the role of Au nanoparticles on WO_3, SnO_2, and NiO-based gas sensors *J. Mater. Chem.* A **9** 1159–67

[3] Tai H, Wang S, Duan Z and Jiang Y 2020 Evolution of breath analysis based on humidity and gas sensors: potential and challenges *Sens. Actuators* B **318** 128104

[4] Li X, Xu J, Jiang Y, He Z, Liu B, Xie H, Li H, Li Z, Wang Y and Tai H 2020 Toward agricultural ammonia volatilization monitoring: a flexible polyaniline/$Ti_3C_2T_x$ hybrid sensitive films based gas sensor *Sens. Actuators* B **316** 128144

[5] Dey A 2018 Semiconductor metal oxide gas sensors: a review *Mater. Sci. Eng.* B **229** 206–17

[6] Cho I, Kang K, Yang D, Yun J and Park I 2017 Localized liquid-phase synthesis of porous SnO_2 nanotubes on MEMS platform for low-power, high performance gas sensors *ACS Appl. Mater. Interfaces* **9** 27111–9

[7] Cho I, Sim Y C, Cho M, Cho Y H and Park I 2020 Monolithic micro light-emitting diode/metal oxide nanowire gas sensor with microwatt-level power consumption *ACS Sens.* **5** 563–70

[8] Choi K W, Jo M S, Lee J S, Yoo J Y and Yoon J B 2020 Perfectly aligned, air-suspended nanowire array heater and its application in an always-on gas sensor *Adv. Funct. Mater.* **30** 2004448

[9] Long H, Harley-Trochimczyk A, Cheng S, Hu H, Chi W S, Rao A, Carraro C, Shi T, Tang Z and Maboudian R 2016 Nanowire-assembled hierarchical $ZnCo_2O_4$ microstructure integrated with a low-power microheater for highly sensitive formaldehyde detection *ACS Appl. Mater. Interfaces* **8** 31764–71

[10] Kang Y, Kim K, Cho B, Kwak Y and Kim J 2020 Highly sensitive detection of benzene, toluene, and xylene based on CoPP-functionalized TiO_2 nanoparticles with low power consumption *ACS Sens.* **5** 754–63

[11] Prajesh R, Jain N and Agarwal A 2016 Low power highly sensitive platform for gas sensing application *Microsyst. Technol.* **22** 2185–92

[12] Chen Y, Li M, Yan W, Zhuang X, Ng K W and Cheng X 2021 Sensitive and low-power metal oxide gas sensors with a low-cost microelectromechanical heater *ACS Omega* **6** 1216–22

[13] Kang M, Cho I, Park J, Jeong J, Lee K, Lee B, Del Orbe Henriquez D, Yoon K and Park I 2022 High accuracy real-time multi-gas identification by a batch-uniform gas sensor array and deep learning algorithm *ACS Sens.* **7** 430–40

[14] Yun J, Ahn J H, Moon D I, Choi Y K and Park I 2019 Joule-heated and suspended silicon nanowire based sensor for low-power and stable hydrogen detection *ACS Appl. Mater. Interfaces* **11** 42349–57

[15] Kang K, Yang D, Park J, Kim S, Cho I, Yang H H, Cho M, Mousavi S, Choi K H and Park I 2017 Micropatterning of metal oxide nanofibers by electrohydrodynamic (EHD) printing towards highly integrated and multiplexed gas sensor applications *Sens. Actuators* B **250** 574–83

[16] Choi K W, Lee J S, Seo M H, Jo M S, Yoo J Y, Sim G S and Yoon J B 2019 Batch-fabricated CO gas sensor in large-area (8-inch) with sub-10 mW power operation *Sens. Actuators* B **289** 153–9

[17] Hsieh C H, Lin T W, Juang F R and Yu Huang I 2023 Micro-gas sensor with a suspended micro-heater for ammonia gas detection *J. Micromech. Microeng.* **33** 015004

[18] Gaiardo A *et al* 2021 Optimization of a low-power chemoresistive gas sensor: predictive thermal modelling and mechanical failure analysis *Sensors* **21** 1–19

[19] Vasiliev A A, Lipilin A S, Mozalev A M, Lagutin A S, Pisliakov A V, Zaretskiy N P, Samotaev N N and Sokolov A V 2011 Gas sensors based on MEMS structures made of ceramic ZrO_2 /Y_2O_3 material *Proc. SPIE* **8066** 80660N

[20] Chang W Y and Hsihe Y S 2016 Multilayer microheater based on glass substrate using MEMS technology *Microelectron. Eng.* **149** 25–30

[21] Wang S, Tian Y, Wang C, Hang C, Zhang H, Huang Y and Zheng Z 2019 One-step fabrication of copper nanopillar array-filled AAO films by pulse electrodeposition for anisotropic thermal conductive interconnectors *ACS Omega* **4** 6092–6

[22] Lee J, Kim Y, Jung U and Chung W 2013 Thermal conductivity of anodized aluminum oxide layer: the effect of electrolyte and temperature *Mater. Chem. Phys.* **141** 680–5

[23] Vasiliev A A *et al* 2016 Non-silicon MEMS platforms for gas sensors *Sens. Actuators* B **224** 700–13

[24] Roslyakov I V, Napolskii K S, Stolyarov V S, Karpov E E, Ivashev A V and Surtaev V N 2018 A thin-film platform for chemical gas sensors *Russ. Microelectron.* **47** 226–33

[25] Park S, Lee D, Byun S, Yoo H, Park D W, Hwang W and Choi J 2016 Pt heating electrode for microheater based on electrochemically prepared anodic porous alumina *Int. J. Electrochem. Sci.* **11** 7401–11

[26] Vasiliev A A, Pavelko R G, Gogish-Klushin S Y, Kharitonov D Y, Gogish-Klushina O S, Sokolov A V, Pisliakov A V and Samotaev N N 2008 Alumina MEMS platform for impulse semiconductor and IR optic gas sensors *Sens. Actuators* B **132** 216–23

[27] Tang W, Chen Z, Song Z, Wang C, Wan Z, Chan C L J, Chen Z, Ye W and Fan Z 2022 Microheater integrated nanotube array gas sensor for parts-per-trillion level gas detection and single sensor-based gas discrimination *ACS Nano* **16** 10968–78

[28] Song Z *et al* 2021 Wireless self-powered high-performance integrated nanostructured-gas-sensor network for future smart homes *ACS Nano* **15** 7659–67

[29] Lee J H, Park M S, Jung H, Choe Y S, Kim W, Song Y G, Kang C Y, Lee H S and Lee W 2020 Selective C_2H_2 detection with high sensitivity using SnO_2 nanorod based gas sensors integrated with a gas chromatography *Sens. Actuators* B **307** 127598

[30] Lei G, Lou C, Liu X, Xie J, Li Z, Zheng W and Zhang J 2021 Thin films of tungsten oxide materials for advanced gas sensors *Sens. Actuators* B **341** 129996

[31] Chang K S, Yang S C, Kim J Y, Kook M H, Ryu S Y, Choi H Y and Kim G H 2012 Precise temperature mapping of GaN-based LEDs by quantitative infrared micro-thermography *Sensors* **12** 4648–60

[32] Chen R, Wang J and Xiang L 2018 Facile synthesis of mesoporous ZnO sheets assembled by small nanoparticles for enhanced NO_2 sensing performance at room temperature *Sens. Actuators* B **270** 207–15

[33] Song Y, Chen F, Zhang Y, Zhang S, Liu F, Sun P, Yan X and Lu G 2019 Fabrication of highly sensitive and selective room-temperature nitrogen dioxide sensors based on the ZnO nanoflowers *Sens. Actuators* B **287** 191–8

[34] Yildirim D, Li G P and Bachman M 2016 Deep, high aspect ratio etches in alumina films for MEMS and advanced packages *Proc.—Electronic Components and Technology Conf.* pp 1918–23

[35] Borca-Tasciuc D A and Chen G 2005 Anisotropic thermal properties of nanochanneled alumina templates *J. Appl. Phys.* **97** 084303

[36] Horiuchi M, Matsuda Y, Tokutake Y, Fukasawa R and Kobayashi T 2013 Copper-filled anodic aluminum oxide: a potential substrate material for a high density interconnection *Proc.—Electronic Components and Technology* pp 937–43

[37] Chan H-Y, Zhang Z-H, Bachman M and G-p L 2019 Porous anodic aluminum oxide interposer: fabrication, characterization, and evaluation *ECS J. Solid State Sci. Technol.* **8** 18–23

[38] Abad B, Maiz J and Martin-Gonzalez M 2016 Rules to determine thermal conductivity and density of anodic aluminum oxide (AAO) membranes *J. Phys. Chem.* C **120** 5361–70

[39] Tsyntsaru N, Kavas B, Sort J, Urgen M and Celis J P 2014 Mechanical and frictional behaviour of nano-porous anodized aluminium *Mater. Chem. Phys.* **148** 887–95

[40] Burgués J and Marco S 2018 Low power operation of temperature-modulated metal oxide semiconductor gas sensors *Sensors* **18** 339

[41] Mineo G, Scuderi M, Bruno E and Mirabella S 2022 Engineering hexagonal/monoclinic WO_3 Phase junctions for improved electrochemical hydrogen evolution reaction *ACS Appl. Energy Mater.* **5** 9702–10

[42] Chen F, Yang M, Wang X, Song Y, Guo L, Xie N, Kou X, Xu X, Sun Y and Lu G 2019 Template-free synthesis of

cubic-rhombohedral-In$_2$O$_3$ flower for ppb level acetone detection *Sens. Actuators* B **290** 459–66

[43] Katoch A, Sun G J, Choi S W, Byun J H and Kim S S 2013 Competitive influence of grain size and crystallinity on gas sensing performances of ZnO nanofibers *Sens. Actuators* B **185** 411–6

[44] Yan S and Wu Q 2015 A novel structure for enhancing the sensitivity of gas sensors—α-Fe$_2$O$_3$ nanoropes containing a large amount of grain boundaries and their excellent ethanol sensing performance *J. Mater. Chem.* A **3** 5982–90

[45] Harley-Trochimczyk A, Rao A, Long H, Zettl A, Carraro C and Maboudian R 2017 Low-power catalytic gas sensing using highly stable silicon carbide microheaters *J. Micromech. Microeng.* **27** 045003

[46] Hsueh T J, Peng C H and Chen W S 2020 A transparent ZnO nanowire MEMS gas sensor prepared by an ITO micro-heater *Sens. Actuators* B **304** 127319

[47] Tommasi A, Cocuzza M, Perrone D, Pirri C F, Mosca R, Villani M, Delmonte N, Zappettini A, Calestani D and Marasso S L 2017 Modeling, fabrication and testing of a customizable microma-chined hotplate for sensor applications *Sensors* **17** 62

[48] Prasad M 2015 Design, development and reliability testing of a low power bridge-type micromachined hotplate *Microelectron. Reliab.* **55** 937–44

[49] Subhani K N, Khandare S, VeeraPandi N and Bhat K N 2022 Localized suspended micro-heater structure using dry etching for sensing and actuation application *J. Manuf. Process.* **83** 281–9